Equatorial locations of water on Mars:
Improved resolution maps based on Mars Odyssey Neutron Spectrometer data

Jack T. Wilson[a,1], Vincent R. Eke[a], Richard J. Massey[a], Richard C. Elphic[b], William C. Feldman[c], Sylvestre Maurice[d], Luís F. A. Teodoro[e]

[a]*Institute for Computational Cosmology, Department of Physics, Durham University, Science Laboratories, South Road, Durham DH1 3LE, UK*
[b]*Planetary Systems Branch, NASA Ames Research Center, MS 2453, Moffett Field, CA,94035-1000, USA*
[c]*Planetary Science Institute, Tucson, AZ 85719, USA*
[d]*IRAP-OMP, Toulouse, France*
[e]*BAER, Planetary Systems Branch, Space Sciences and Astrobiology Division, MS 245-3, NASA Ames Research Center, Moffett Field, CA 94035-1000, USA*

Abstract

We present a map of the near subsurface hydrogen distribution on Mars, based on epithermal neutron data from the Mars Odyssey Neutron Spectrometer. The map's spatial resolution is approximately improved two-fold via a new form of the pixon image reconstruction technique. We discover hydrogen-rich mineralogy far from the poles, including ~10 wt. % water equivalent hydrogen (WEH) on the flanks of the Tharsis Montes and >40 wt. % WEH at the Medusae Fossae Formation (MFF). The high WEH abundance at the MFF implies the presence of bulk water ice. This supports the hypothesis of recent periods of high orbital obliquity during which water ice was stable on the surface. We find the young undivided channel system material in southern Elysium Planitia to be distinct from its surroundings and exceptionally dry; there is no evidence of hydration at the location in Elysium Planitia suggested to contain a buried water ice sea. Finally, we find that the sites of recurring slope lineae (RSL) do not correlate with subsurface hydration. This implies that RSL are not fed by large, near-subsurface aquifers, but are instead the result of either small (<120 km diameter) aquifers, deliquescence of perchlorate and chlorate salts or dry, granular flows.

Keywords:
Mars ; Mars, surface ; Neutron spectroscopy ; Image reconstruction

1. Introduction

The main goal of the Mars Odyssey Neutron Spectrometer (MONS) is to determine the major near-surface reservoirs of hydrogen on Mars (Feldman et al., 2004b). Knowing the present distribution of water in the Martian near-subsurface is important for several reasons: it allows inferences about the past and present climate to be drawn, which, in turn, give information about the dynamic history of Mars and the possibility of the past, or present, existence of life. Additionally, understanding the small-scale distribution of water is important for landing site selection for missions looking for signs of life or exploring in-situ resource utilisation (Squyres, 2011). MONS data have been used to map the hydrogen content of the Martian near-subsurface (Feldman et al., 2002; Tokar et al., 2002; Feldman et al., 2004b) on ~ 550 km scales (Teodoro et al., 2013). Hydrogen rich deposits, with WEH content > 25 wt. %, were found poleward of ±60°, which were interpreted as water-ice buried under a layer of desiccated soil (Feldman et al., 2002). Additional low-latitude hydrogen deposits were observed at Arabia Terra and Elysium Planitia (Feldman et al., 2002) with 9.5±1.5 wt. % WEH (Feldman et al., 2004a). Water ice should

not be stable equatorward of ± 30° (Mellon and Jakosky, 1993), which has led to the suggestion that these equatorial hydrogen deposits are in the form of hydrated minerals (Feldman et al., 2002).

The ~ 550 km spatial resolution of the MONS instrument suppresses smaller-scale features in the MONS data, and the inferred hydrogen distribution. It also results in a reduction in the dynamic range of the data, leading to an underestimate in the wt. % WEH content of small hydrogen-rich areas. The previously inferred WEH abundances for equatorial features will have been underestimated because of this effect. In this paper we will develop and apply an image reconstruction technique based on the pixon method, which has been used to successfully reconstruct planetary data (Lawrence et al., 2007; Elphic et al., 2007; Eke et al., 2009; Wilson et al., 2015), to improve the resolution of the global MONS data set in a way that is robust to noise. This will be the first application of a Bayesian image reconstruction technique to a globally defined remotely-sensed planetary data set.

We will focus on a few locations that have been proposed to contain water in the equatorial regions of Mars deposited in the geologically recent past. This water is hypothesised to have been deposited during past periods of high orbital obliquity when the water ice currently at the poles becomes unstable and is ultimately deposited elsewhere (Forget et al., 2006).

---

[1]Present address: The Johns Hopkins Applied Physics Laboratory, 11100 Johns Hopkins Road, Laurel, MD 20723, USA

Evidence for equatorial hydration is both morphological (Head and Weiss, 2014) and compositional (Feldman et al., 2004b), and is seen at both the Medusae Fossae Formation (MFF) and the Tharsis Montes.

The MFF is a discontinuous geological unit of easily erodible material that stretches ~ 1000 km across equatorial latitudes, along the boundary of the northern lowlands and southern highlands, located in both Elysium and Amazonis Planitiae. The origin of the MFF is uncertain. Proposed explanations include consolidated pyroclastic deposits (Scott and Tanaka, 1982) and aeolian sediments with ice-rich material (Head and Kreslavsky, 2004), similar to that found in the polar layered deposits (Schultz and Lutz, 1988), laid down during periods of high orbital obliquity. Radar sounding using the MARSIS instrument onboard ESA's Mars Express has been used to measure the dielectric constant of the MFF material and found it to be consistent with the MFF containing a large component of water ice or anomalously low density soil (Watters et al., 2007). It may be possible to distinguish between these two mechanisms using neutron derived hydrogen abundances.

Evidence, in the form of surface morphology and cratering, for late Amazonian tropical mountain glaciers on the northwestern flanks of the Tharsis Montes and Olympus Mons has been detailed extensively using observations from the Mars Express, Mars Global Surveyor and Mars Odyssey orbiters (Head and Marchant, 2003; Shean et al., 2005, 2007). The production of such glaciers at equatorial Mars today is impossible given the current climatic conditions. Thus, the existence of these glaciers is interpreted to be the result of the migration of volatiles (chiefly water) from the poles to the equator during past periods of high orbital obliquity. Climate models predict the accumulation of ice on the north-western slopes of these mountains, during hypothesised periods of high obliquity, due to the adiabatic cooling of moist polar air (Forget et al., 2006; Madeleine et al., 2009).

The extent to which these equatorial deposits remain and the form in which they are present are not yet settled questions. Campbell et al. (2013) see no evidence for buried ice at Pavonis Mons using the Shallow Radar (SHARAD) instrument onboard the Mars Reconnaissance Orbiter. However, morphological evidence is presented by Head and Weiss (2014) in the form of fresh ring-mold craters at both Pavonis and Arsia Mons, which is suggestive of the presence of buried ice today or in the very recent past.

The utility of this data set in constraining the distribution of water on the scale of the tropical mountain glaciers has been limited by its relatively poor spatial resolution due to the ~ 550 km full width at half maximum, FWHM, footprint of the MONS. Jansson's method was used by Elphic et al. (2005) to perform image reconstruction on the MONS data at Tharsis. However, it is known that this method amplifies noise and may introduce spurious features (Prettyman et al., 2009).

We will use our improved resolution map of the epithermal neutron count rate across the entire surface of Mars to look for evidence of buried, non-polar hydrogen in the form of both hydrated minerals and water ice at the Tharsis Montes and the Medusae Fossae Formation. In addition, we will examine several non-polar sites where water is suggested to be present in some form: Meridiani Planum, Elysium Planitia and the southern-mid latitudes, where RSL are observed. The increase in resolution over the unreconstructed MONS data allows better correspondence between structures in the neutron data and features in surface imagery, thus enabling a more robust geophysical interpretation.

In the next section we describe the modifications made to the pixon method and the new algorithm that has been developed. In section 3 we discuss the MONS data used in this study, along with the properties of the instrument, before presenting the results of the reconstructions in section 4. Small scale features that emerge in the reconstructions are described in sections 5 and 6. Finally, we conclude in section 7.

2. Methods

In this section we will describe a new version of the pixon image reconstruction technique, adapted for use on the sphere. The pixon method is a Bayesian image reconstruction technique, in which pixels are grouped together to form 'pixons' (Pina and Puetter, 1993; Eke, 2001). It is motivated by considering the posterior probability

$$P(\hat{I}, M|D) = \frac{P(D|\hat{I}, M)P(\hat{I}|M)P(M)}{P(D)}, \qquad (1)$$

where $\hat{I}$ is the reconstructed image and M is the model, which describes the relationship between $\hat{I}$ and the data, including the point spread function, PSF, and the basis in which the image is represented. As the data are already taken, $P(D)$ is not affected by anything we can do and is therefore constant. Additionally, to avoid bias, $P(M)$ is assumed to be uniform. This assumption leaves two terms: the first, $P(D|\hat{I}, M)$, is the likelihood of the data given a particular reconstruction and model, calculated using a misfit statistic. The second term, $P(\hat{I}|M)$, is the image prior. The grouping of pixels into pixons greatly reduces the number of degrees of freedom in the reconstructed image, improving the image prior. The most likely reconstruction is that containing fewest pixons that is still able to provide a sufficiently good fit to the data.

2.1. Locally adaptive pixon reconstruction

Previous versions of the pixon method imposed a strict maximum entropy constraint on the solution (Pina and Puetter, 1993; Eke, 2001), in order to simplify the maximization of the posterior by reducing the parameter space that is to be explored. Here we make no such requirement, which will allow the creation of previously inaccessible and more likely reconstructions.

As in the maximum entropy pixon method the reconstructed count-rate map, $\hat{I}$, is constructed by convolving a 'pseudoimage', H, with a Gaussian kernel, K, whose width, δ, may vary across the image, i.e.

$$\hat{I}(\mathbf{x}) = (K_{\delta(\mathbf{x})} * H)(\mathbf{x}). \qquad (2)$$

Initially the smoothing scale, or pixon width, $\delta(\mathbf{x})$, is large. The final value is determined for each pixel using an iterative procedure, which includes the calculation of a newly defined local misfit statistic. In practice a finite set of distinct pixon sizes is used as this keeps the time of a single calculation of the global misfit statistic, E_R, down to $O(n_{\mathrm{pixels}} \log n_{\mathrm{pixels}})$ (i.e. that of a fast Fourier transform), where n_{pixels} is the number of pixels in the image, whereas if the pixon size were allowed to vary continuously then the time would be $O(n_{\mathrm{pixels}}^2 \log n_{\mathrm{pixels}})$. In order to generate $\hat{I}$ we interpolate linearly between the images based on the two pixon sizes closest to those required for each pixel.

The following subsection describes the structure of the locally adaptive pixon algorithm before the details of the misfit statistic and prior calculation are detailed.

2.1.1. Structure of the locally adaptive pixon algorithm

Our goal is to maximize the posterior probability (equation (1)) whilst ensuring that the residual field should be indistinguishable from a random Gaussian field. We do this using an iterative procedure with two stages in each iteration (figure 1). Firstly, for a given pixon size distribution the values in the pseudoimage are adjusted to minimize the global misfit statistic (see section 2.1.2) using the Polak-Ribière conjugate gradient minimization algorithm (Press et al., 1992). Secondly, we calculate the value of the posterior and, for each pixel in the datagrid, the local misfit statistic (section 2.1.3). These local misfit statistics are then ordered to form their cumulative distribution function (CDF). The difference, in each pixel, between the actual and expected, χ^2-distributed, CDF is then used to modify the pixon size in the same pixel. The change in pixon width is directly proportional to this difference, with the constant of proportionality determined empirically such that structure appears in the image sufficiently slowly to avoid introducing spurious features.

The combination of global misfit statistic minimization and pixon size modification is repeated, starting with large pixons and consequently a flat, constant reconstructed image everywhere, until the posterior probability stops increasing.

2.1.2. The global misfit statistic, E_R

The misfit statistic is derived from the reduced residuals between the data and the blurred model,

$$R(\mathbf{x}) = \frac{D(\mathbf{x}) - (\hat{I} * B)(\mathbf{x})}{\sigma(\mathbf{x})}, \qquad (3)$$

where $\sigma(\mathbf{x})$ is the anticipated statistical noise in pixel $\mathbf{x}$. Rather than using $\chi^2 = \sum R^2$, we adopt E_R from Pina and Puetter (1992) as the misfit statistic. This statistic is defined as

$$E_R = \sum_{\mathbf{y}} A_R(\mathbf{y})^2, \qquad (4)$$

where A_R is the autocorrelation of the residuals, $A_R(\mathbf{y}) = \int R(\mathbf{x}) R(\mathbf{x} + \mathbf{y}) \mathrm{d}\mathbf{x}$ for a 2-dimensional pixel separation, or lag, of $\mathbf{y}$. The benefit of minimizing E_R, over the more conventional χ^2, is that doing so suppresses spatial correlations in the residuals, preventing spurious features being formed by the reconstruction process. Pina and Puetter (1992) recommend that the
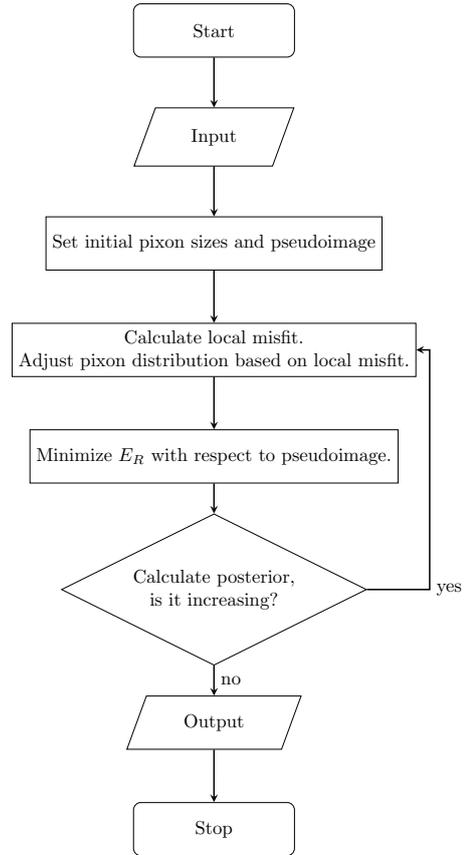

Figure 1: A flow chart showing the locally adaptive pixon image reconstruction algorithm.

autocorrelation terms defining E_R should be those corresponding to pixel separations smaller than the instrumental PSF. For a well-sampled PSF this means many different pixel lags. However, for the reconstructions we have attempted, there is negligible difference between those including different numbers of pixel lags. We therefore use only terms with adjacent pixels (including diagonally adjacent pixels in 2D) to speed up the computation. Although each pixel is adjacent to eight others the symmetry implies that $A_R(\mathbf{y}) = A_R(-\mathbf{y})$, so only the four distinct terms need be included when calculating E_R.

Prior to this work the pixon method has been implemented only on flat planes. When calculating E_R on a spherical surface we decided to map the sphere to a flat (i.e. Gaussian curvature equal to zero) torus. This is done via an equirectangular projection of the sphere to a square Cartesian plane (by extending the regular parameterization of the sphere to $0 < \theta < 2\pi$, $0 < \phi < 2\pi$) and identifying opposite edges. This mapping leaves the details of the calculation, including the use of FFTs for fast convolution, unchanged from the flat 2D case. However, as the lag terms included in E_R cover a certain number of pixels this mapping has the side effect of mixing the physical scales over which the statistic is defined.

2.1.3. Local misfit statistic, E'_R

To create a local E_R statistic, E'_R, we begin by localizing A_R by multiplying with a kernel, K, such that

$$A'_R(\mathbf{x}, \mathbf{z}) = \int R(\mathbf{y}) R(\mathbf{x} + \mathbf{y}) K(\mathbf{z} - \mathbf{y}) \, d\mathbf{y}, \tag{5}$$

which we can rewrite in a form resembling a convolution, by defining $C_{\mathbf{x}}(\mathbf{y}) = R(\mathbf{y}) R(\mathbf{x} + \mathbf{y})$, as

$$A'_R(\mathbf{x}, \mathbf{z}) = \int C_{\mathbf{x}}(\mathbf{y}) K(\mathbf{z} - \mathbf{y}) \, d\mathbf{y}. \tag{6}$$

We are free to choose the kernel and for ease of calculation select a gaussian, the width of which should be larger than the largest pixon width so that it is the pixon size, and not its gradient, that sets the smoothing scale in the reconstruction. For use in determining pixon widths we need to know the distribution of A'_R. Noting that $C_{\mathbf{x}}(\mathbf{y})$ has a normal product distribution with width one and applying the central limit theorem allows one to deduce that A'_R must have a standard normal distribution so E'_R obeys a χ^2 distribution.

When convolving in angular space we should define (using equation (B.1)).

$$A'_R(\mathbf{x}, \omega(\mathbf{z})) = \left(\frac{C_{\mathbf{x}}}{a} * K \right)(\omega(\mathbf{z})), \tag{7}$$

and

$$E'_R(\mathbf{z}) = \sum_{\mathbf{y}} \frac{A'^2_R(\mathbf{y}, \mathbf{z})}{\sigma^2_{A'_R}(\mathbf{z})}, \tag{8}$$

where $\sigma^2_{A'_R}$ can be deduced by analogy with a random walk i.e.

$$\sigma^2_{A'_R}(\mathbf{z}) = \int K^2(\mathbf{z} - \mathbf{y}) \, d\mathbf{y}$$
$$= \left(\frac{1}{a} * K^2 \right)(\omega(\mathbf{z})). \tag{9}$$

2.1.4. Prior calculation

Counting arguments show that, in the pixon method, the prior is given by

$$\ln(P(I|M)) \approx N \ln\left(\frac{N}{n} \right) + \frac{1}{2} \ln(N) - \frac{n-1}{2} \ln(2\pi) - \sum_{i=1}^{n} \left(N_i + \frac{1}{2} \right) \ln(N_i), \tag{10}$$

where N is total amount of information in the image, N_i the information content of pixon i and n is the number of pixons (see e.g. Eke (2001) for a full derivation). In the maximum entropy pixon method the content of each pixon was defined to be equal, so its explicit numerical calculation is never necessary (i.e. $N_i = N/n$). However, our new pixons are not only inhomogeneous but there needn't be an integer number, with pixon number defined as

$$n = \sum_{\mathbf{x}} \frac{1}{2\pi \delta(\mathbf{x})^2}, \tag{11}$$

i.e. the number of independent degrees of freedom in the image. For the case of a non-integer number of pixons we choose to weight the contribution of the final non-integer pixon, such that the natural logarithm of the prior (using Stirling's approximation) becomes

$$\ln(P(I|M)) \approx N \ln\left(\frac{N}{n} \right) + \frac{1}{2} \ln(N) - \frac{n-1}{2} \ln(2\pi)$$
$$- \sum_{i=1}^{\lfloor n \rfloor} \left(N_i + \frac{1}{2} \right) \ln(N_i) - (n - \lfloor n \rfloor) \left(\left(N_n + \frac{1}{2} \right) \ln(N_n) \right), \tag{12}$$

where N_n is the information in the final fraction of a pixon scaled up to the size it would be if it were filling a whole pixon.

3. Data

Approximately 3.5 Martian years of the time-series MONS prism-1 (Maurice et al., 2011) observations from JD 2452324.125388 (just before the start of Mars Year 26) until JD 2454922.577436 are used in this study. Prism-1 is the nadir facing detector on MONS and is most sensitive to epithermal neutrons. In this paper we restrict our attention to the 'frost-free' data, for which we use the same definition as Maurice et al. (2011) i.e. those data taken at a location (in time and space) in which the CO_2 area density in the NASA Ames GCM is less than 0.2 gcm^{-1}.

As Mars Odyssey is in a near-polar orbit we chose to use an equirectangular pixelization, which results in approximately the same number of observations in each pixel. The density of the pixelation is chosen so that the PSF is well sampled. In this work we use a square, 0.5°×0.5°, grid of pixels in a equirectangular projection. The statistical errors within a pixel are determined, empirically, by calculating the scatter between repeat observations in the observed count rate within the pixel. It was necessary to estimate the noise amplitude per pixel empirically as the various corrections applied to the data, for atmospheric thickness, cosmic ray flux, and spacecraft latitude and altitude, resulted in the data no longer possessing Poisson statistics (Maurice et al., 2011).
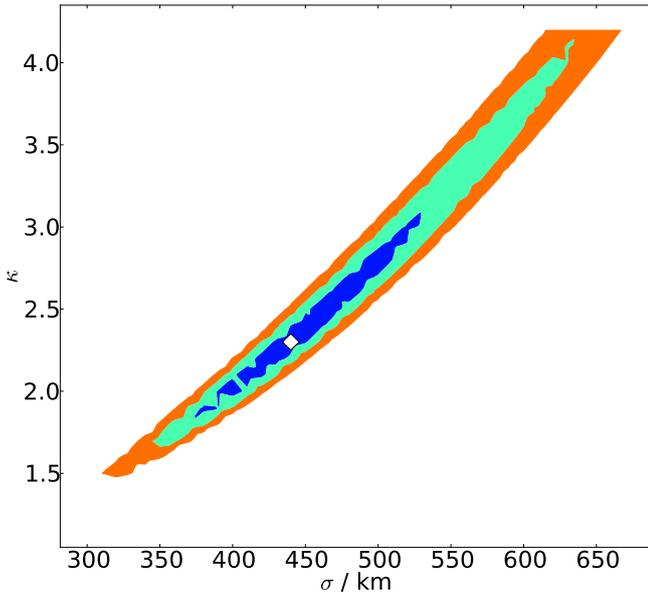
Figure 2: Constraints on the parameters in the PSF. The parameters are those in equation 13. The white diamond shows the best-fit reconstruction with minimum χ^2. Coloured regions enclose probabilities of 68%/95%/99.7%, determined using $\Delta\chi^2 = \chi^2 - \chi^2_{\min}$.

3.1. Assumed instrumental properties

As a starting point for our estimation of the MONS PSF we have taken the calculated prism-1 spatial response of the MONS instrument to a circular feature with 5 degree diameter from Prettyman et al. (2009). This calculation of the response involved the creation of a detailed numerical model of the Martian surface and atmosphere and the Mars Odyssey spacecraft. The production of neutrons via cosmic ray interaction with the Martian atmosphere and surface and their subsequent transport within the surface, atmosphere and exosphere and detection within the spacecraft was performed using the Monte Carlo N-Particle eXtended (MCNPX) transport code. To convert this 'disk spread function' to the instrumental PSF, we calculated the result of convolving a 5° diameter disk with various trial PSFs, assuming that the PSF is azimuthally symmetric about the spacecraft's nadir point. The profile resulting from these convolutions that most closely matches that obtained from the simulations is taken to be the correct PSF. We make the assumption that the PSF can be described by a kappa function, defined as

$$\frac{f(s)}{f(0)} = \left(1 + \frac{s^2}{\sigma^2}\right)^{-\kappa}, \tag{13}$$

where κ and σ are parameters to be determined, s is the arc length from the sub-orbital point and $f(s)$ is the response of the instrument to a source at s. κ functions are often used to model the response of spacecraft-borne gamma ray and neutron detectors (Maurice et al., 2004). The results of this calculation are shown in Fig. 2, from which the best fitting PSF has $\sigma = 440$ km and $\kappa = 2.3$, giving a FWHM of 520km.

4. Results

The global frost-free MONS data and our reconstruction of the underlying field are shown in the two panels of figure 3. Locally adaptive pixon reconstruction of the data leads to an increase in dynamic range of the count rate of nearly 50%, from ~1-11 to ~0-16 counts per second. In addition to the improvement in dynamic range, there is an enhancement in spatial resolution, quantified below. All of the conversions from epithermal neutron count rate to weight % water equivalent hydrogen (wt. % WEH) in this work use the single layer model in Feldman et al. (2004b), i.e. the surface is assumed to be made up of a semi-infinite layer with a constant wt. % WEH content.

4.1. Improvement in resolution

To estimate the resolution of the reconstructed data we consider the two-point correlation function of the reconstruction. Comparing the separation required for the correlation function to drop to a given level allows the effective resolution of the reconstruction to be calculated. The correlation between the count rate at two points (with angular separation θ) on the surface of the planet can be calculated using the relation

$$C(\theta) = \frac{1}{4\pi} \sum_{l=0}^{\infty} (2l+1) C_l P_l \cos\theta, \tag{14}$$

where P_l are the Legendre polynomials and C_l is the power spectrum of the count rate, defined by

$$C_l = \frac{1}{2l+1} \sum_{m=-l}^{l} |a_{lm}|^2, \tag{15}$$

with a_{lm} being the spherical harmonic coefficients defining the count rate field.

This function is plotted in figure 4 for both the data and the reconstructed image. A separation equal to the FWHM of the data (520 km or log(separation) = 2.72) corresponds to a normalized correlation value of log(C(theta)) = -0.06. The reconstructed image reaches this normalized correlation value at a separation of 290 km (or log(separation) = 2.46). Thus the effective FWHM of the map is 290 km rather than 520 km i.e. variations on scales smaller than 290 km are unlikely to be found in our reconstruction. This three fold decrease in effective detector footprint leads to the enhanced dynamic range shown in the reconstruction in figure 3. The value of $C(0)$ i.e. the power on the smallest scales, increases by 40% between the data and reconstruction.

4.2. Estimation of errors in the pixon method

To estimate the systematic and random errors in the pixon method, when applied to the MONS data, we created a set of 10 mock data sets. These mock data were generated by blurring the reconstructed image (figure 3 lower panel) with the PSF and then adding Gaussian noise with σ as determined for the real data. Running the pixon reconstruction algorithm on each of these mock data sets enables the errors in the reconstructed count rate, both statistical and systematic, to be estimated. The upper panel of Figure 5 shows the RMS scatter in
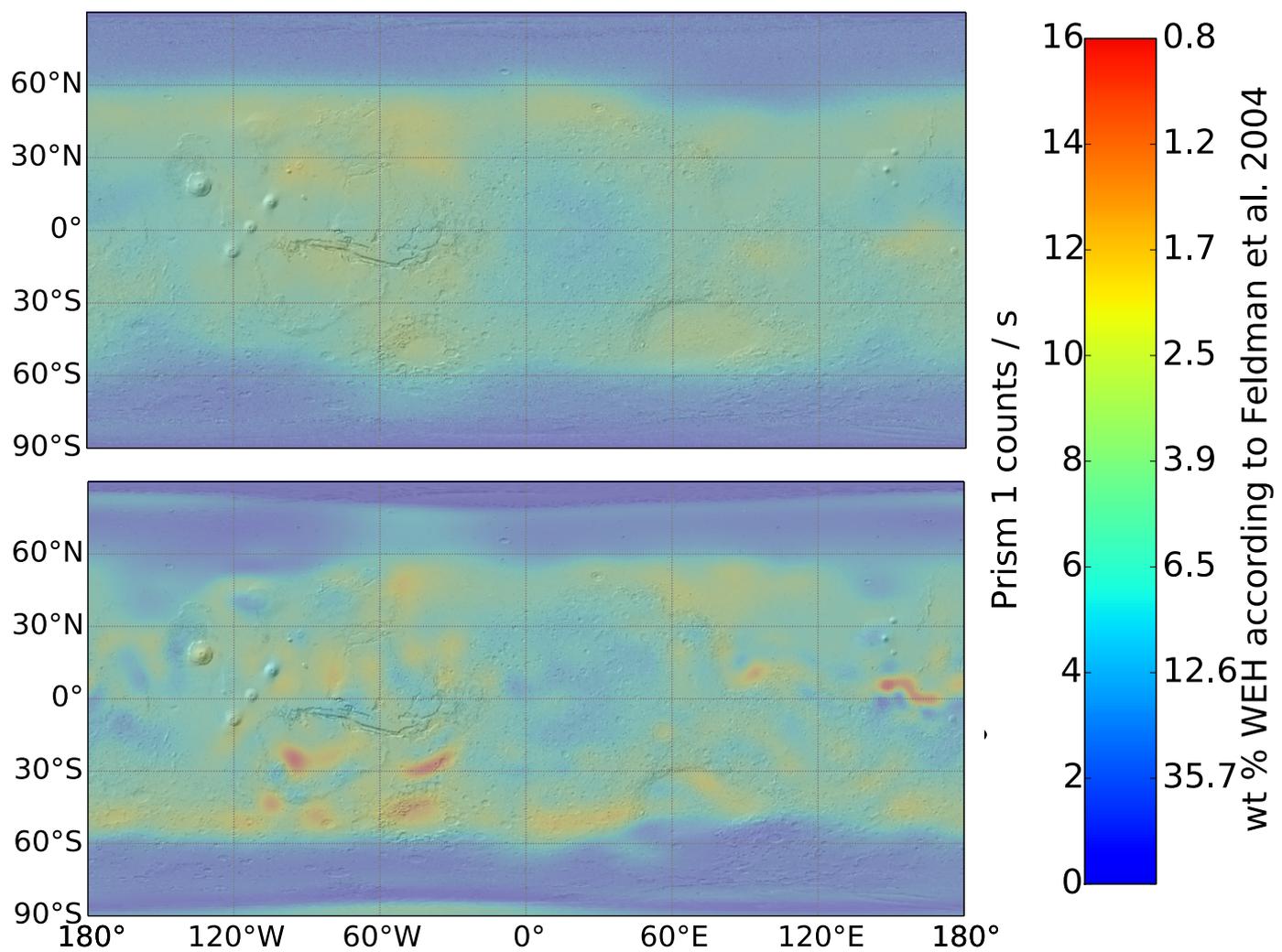
Figure 3: *Top.* The global frost-free MONS prism-1 data, used in the reconstruction. *Bottom.* A global locally-adaptive pixon reconstruction of the MONS prism-1 data. Underlaid on both panels is a MOLA shaded relief map. The colour bar also shows the conversion to wt. % water equivalent hydrogen from Feldman et al. (2004b).
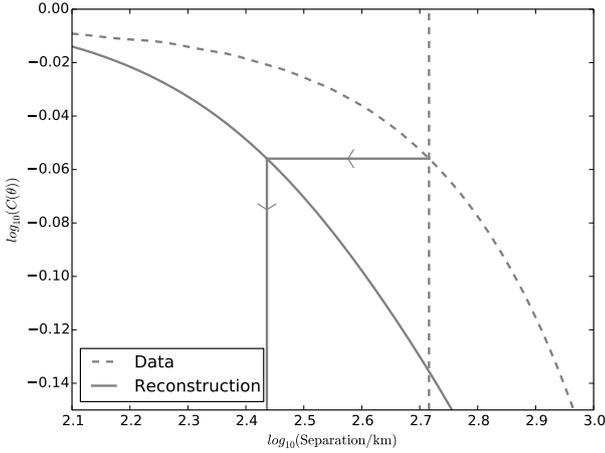
Figure 4: The two point angular correlation function of the MONS data and the reconstruction, normalized to unity at zero separation. The vertical dashed line shows the MONS PSF FWHM scale. The solid vertical line at $\log_{10}(s)$ = 2.46 (or 290 km) shows the separation required for the power in the reconstruction to drop by the same proportion that the power in the data drops at a separation equivalent to the FWHM of the PSF.

each pixel over the 10 reconstructions, a measure of the statistical error in the reconstruction due to noise in the data. Comparison with figure 3 shows the noise to be greatest where the count rate is large or varies quickly, such as at the south polar cap. The global mean statistical error in the reconstructed epithermal count rate is 0.26 counts per second. The average difference between a reconstruction based on mock data from one based on the real data is shown in figure 5 (lower panel). This provides a measure of the systematic errors in the reconstruction method and has a global average of 0.47 counts per second. The regions with highest offset are mostly co-located with those with the largest random errors. The feature at around 0° N, 150° E is particularly discrepant as it features regions of very low and high count rate in close proximity. The inability to completely remove the smoothing effect of convolving with the PSF causes these regions to blend together. The mottling in these images is an artefact related to the size of the pixons.

4.2.1. Limit of detection of increased hydration

To place a limit on the smallest source region that could be detected using the new pixon method we created a series of mock data sets containing circular regions of 100 wt% WEH with various diameters, located in some regions considered in this work, i.e. the southern mid-latitudes, Valles Marineris and the northern mid-latitudes. We then performed reconstructions of these mock data sets and examined the reconstructions to see how large the 100 wt% source region must be before a statistically significant depression in the count rate is seen. The variation of count rate with source size is shown in figure 6, where the error bars show the scatter in a set of ten mock data sets. It can be seen that sources smaller than approximately 60 km in radius do not lead to statistically significant decreases in count rate so are not reliably resolved using this method. There-
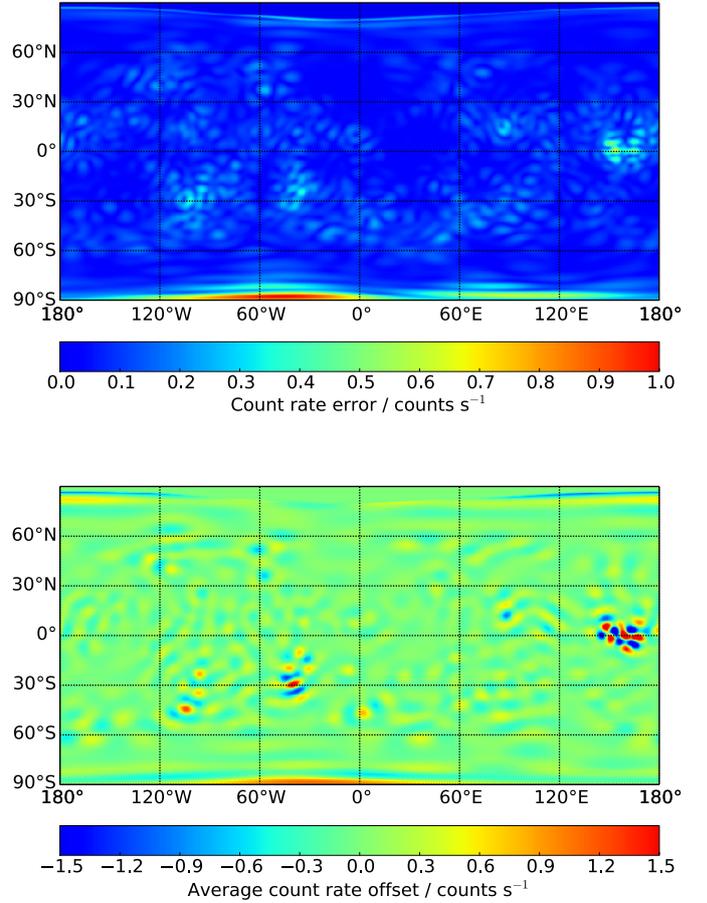

Figure 5: *Top.* The standard deviation of the reconstructed count rate based on 10 mock data sets. *Bottom.* A plot of the average difference, in each pixel, between the mock reconstructions and the true image.
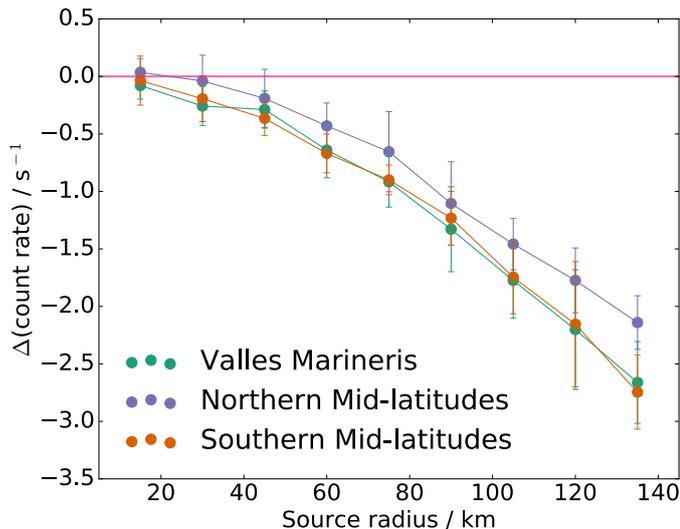
Figure 6: The difference in count rate between reconstructions with 100 wt% WEH sources and those without as a function of source radius. 1σ error bars are calculated from the standard deviation of 10 reconstructions with different noise realizations. The colours correspond to the regions where the sources were inserted. The horizontal line is at count rate difference equal to zero.

fore, we cannot detect near-subsurface water sources smaller than 120 km in diameter.

4.3. Comparing reconstructions with surface measurements

Our reconstructions also enable us to examine the region around Gale crater, the landing site and science target of the Curiosity rover. The Curiosity rover has an active neutron sensor onboard, the Dynamical Albedo of Neutrons (DAN) instrument (Mitrofanov et al., 2012). Unlike for passive, orbital remote sensing, DAN works by illuminating the surface with a pulsed neutron source and then measuring the returned neutron flux to infer composition. This gives us a ground truth against which to compare our reconstructions.

The inferred hydrogen abundance at Gale crater changes little between the raw data and the reconstruction (lower panels in figure 7), being around 8.0 ± 0.4 wt% WEH in both cases. However we find a gradient in the higher resolution reconstruction, with hydration increasing towards the south-east. It is worth noting that these results are discrepant with those obtained by DAN, which suggest an average abundance of 2.1 to 2.7 wt% WEH (Mitrofanov et al., 2014) and those from the High Energy Neutron Detector (HEND) instrument in the Mars Odyssey Gamma Ray Spectrometer suite with 5 wt% WEH (Mitrofanov et al., 2016). It has been suggested that this discrepancy may be the result of the greatly differing sizes of the response functions of the ground and space based detectors (3 m for DAN, 300 km for HEND and 520 km for MONS) and the presence of the rover in a locally dry region (Mitrofanov et al., 2014). However, if this were the correct explanation we may expect that improving the resolution would go some way towards alleviating this discrepancy and we find no evidence of this in our reconstruction. For this explanation to hold, the variation in abundance must be on a scale smaller than the scales

accessible to the reconstruction (i.e. 290 km). Alternatively, the differing mean depths from which the detected neutrons originate may be responsible: DAN is sensitive only to the composition of the top 60 cm of the surface (Mitrofanov et al., 2014), whereas the orbital detectors see up to 1 m into the surface, depending on the soil water abundance. If the deeper regions are more hydrated than the surface then we would expect the orbital detectors to measure larger WEH values than DAN.

5. Possible sites of remnant hydration from periods of high obliquity

We showed, in section 4.1, that pixon reconstruction of the MONS data yields a near two-fold improvement in linear spatial resolution and a 50% increase in dynamic range. Here, we will use these results to examine a series of science targets that have sizes close to or smaller than the MONS PSF and are suggested, or believed, to contain contemporary water ice or hydrated minerals. The selected sites are outlined in figure 8.

In this section we will focus on a few locations that have been proposed to contain water in the equatorial regions of Mars deposited during periods of high orbital obliquity and use the results of the previous section to infer their present hydration.

5.1. The Medusae Fossae Formation: ice or dry, porous rock?

The topography and MONS reconstruction of the MFF are shown in figure 9. The western lobes, Aeolis, Zephyria and Lucus Plana, of the MFF are greatly enriched in hydrogen, with >10 wt. % WEH. At Aeolis Planum the neutron data imply a WEH abundance > 40 wt. %. This is too great an abundance to be explained as hydrous silicates, which have WEH abundances of 10-20 wt. % (Feldman et al., 2004b), so must be buried water ice or hydrated salts. WEH abundances above ~ 26 wt. % cannot be accommodated as ice within soil pore spaces, so if ice is present at the MFF it must be present as bulk ice (Feldman et al., 2011). However, the eastern lobes of the MFF contain little, if any, increased hydration. Geologically, the western lobes are associated with the lower members of the deposit, whereas the eastern lobes corresponds to upper and middle members only (Scott and Tanaka, 1986; Greeley and Guest, 1987). The region of enhanced hydration at 10° S, 165° W is not coincident with the MFF, but does lie on the dichotomy boundary (the line separating the Martian northern lowlands and southern uplands).

At present water ice is unstable at any depth near the Martian equator (Schorghofer and Aharonson, 2005; Schorghofer, 2007). However, Martian orbital obliquity has varied greatly over the past 20 Ma (Laskar et al., 2004). During high obliquity periods the polar water ice caps become unstable and ice may be deposited down to equatorial locations (Forget et al., 2006). Protection of this deposited ice by dust, perhaps containing cemented duricrust layers, could lead to its continued presence today (Feldman et al., 2011; Wang and Ling, 2011).

Our result is consistent with the lower member of the MFF containing ice rich material, which lends weight to the theory that, at least part of, the MFF is a polar layered-like deposit. Salt hydrates could also explain the observations as they have
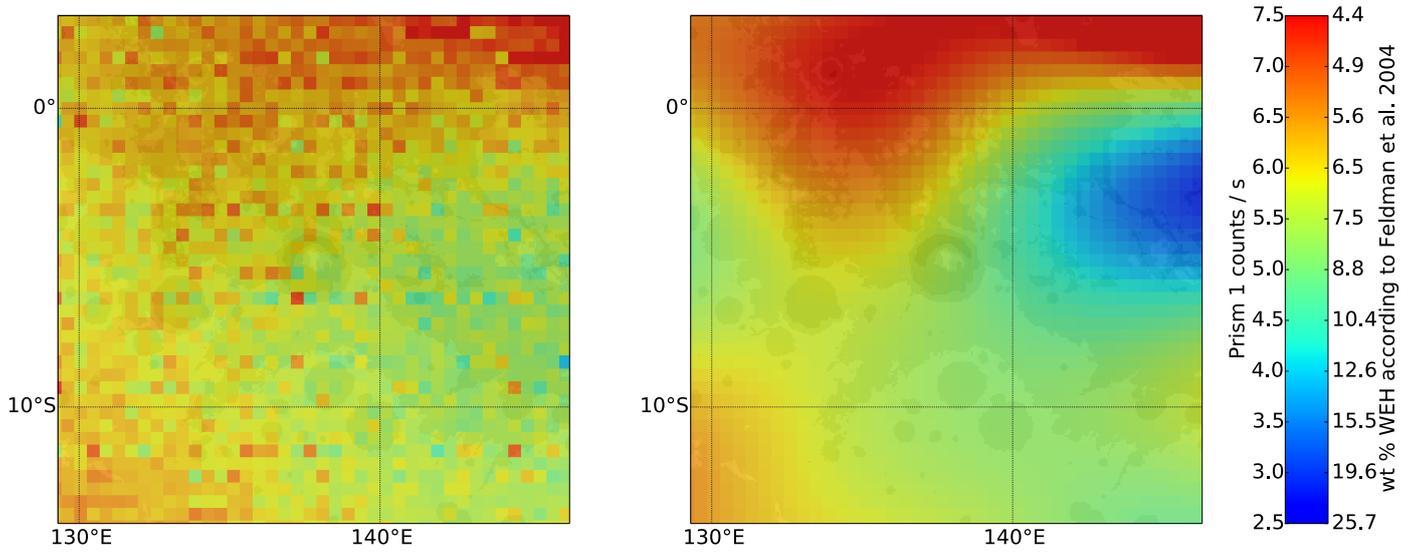
Figure 7: The MONS data (left) and reconstruction (right) in the area around Gale Crater. Underlaid is a MOLA shaded relief map. The colour bars also show the conversion to wt. % water equivalent hydrogen from Feldman et al. (2004b).
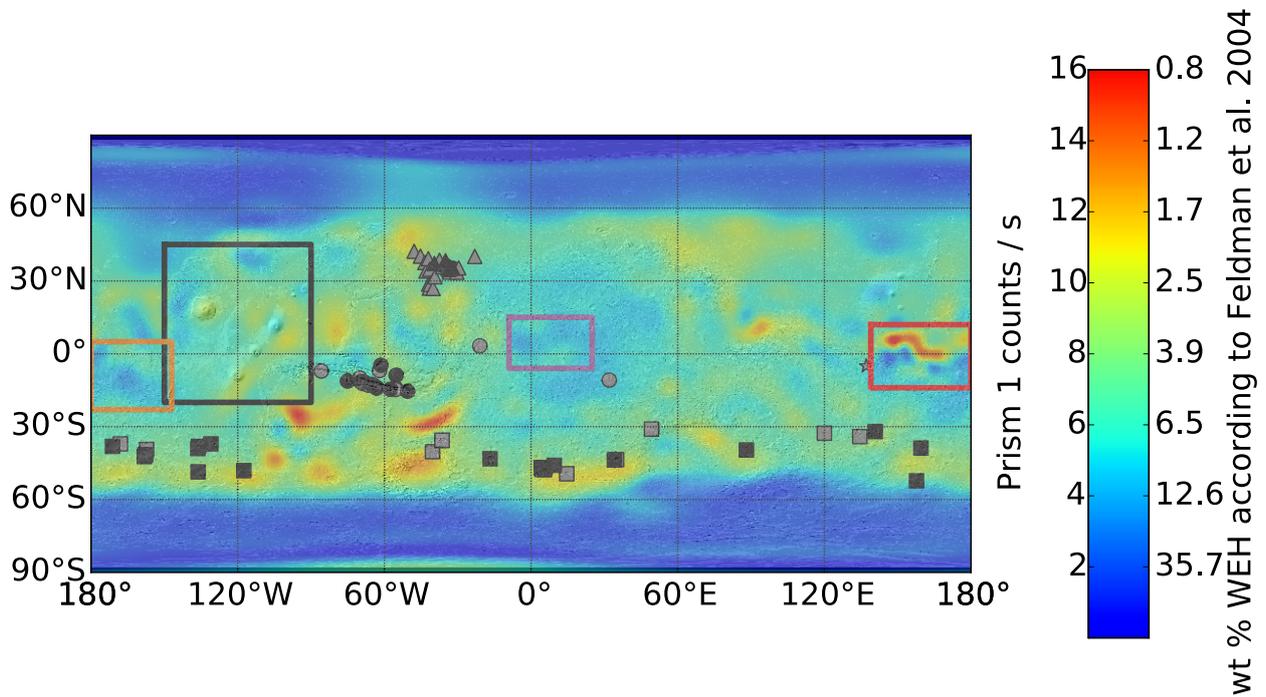

Figure 8: Global MONS reconstruction outlining the regions examined in later sections. The Tharsis Montes, examined in section 5.2, are outlined in black, Elysium planitia and part of the Medusae Fossae Formation, in red, the remaining section of the Medusae Fossae Formation, in orange, and Meridiani Planum in violet. The locations of both confirmed (black) and candidate (grey) RSL are also shown as identified in McEwen et al. (2011) (squares), Stillman et al. (2014) (circles) Stillman et al. (2016) (triangles) and Dundas and McEwen (2015) (star).
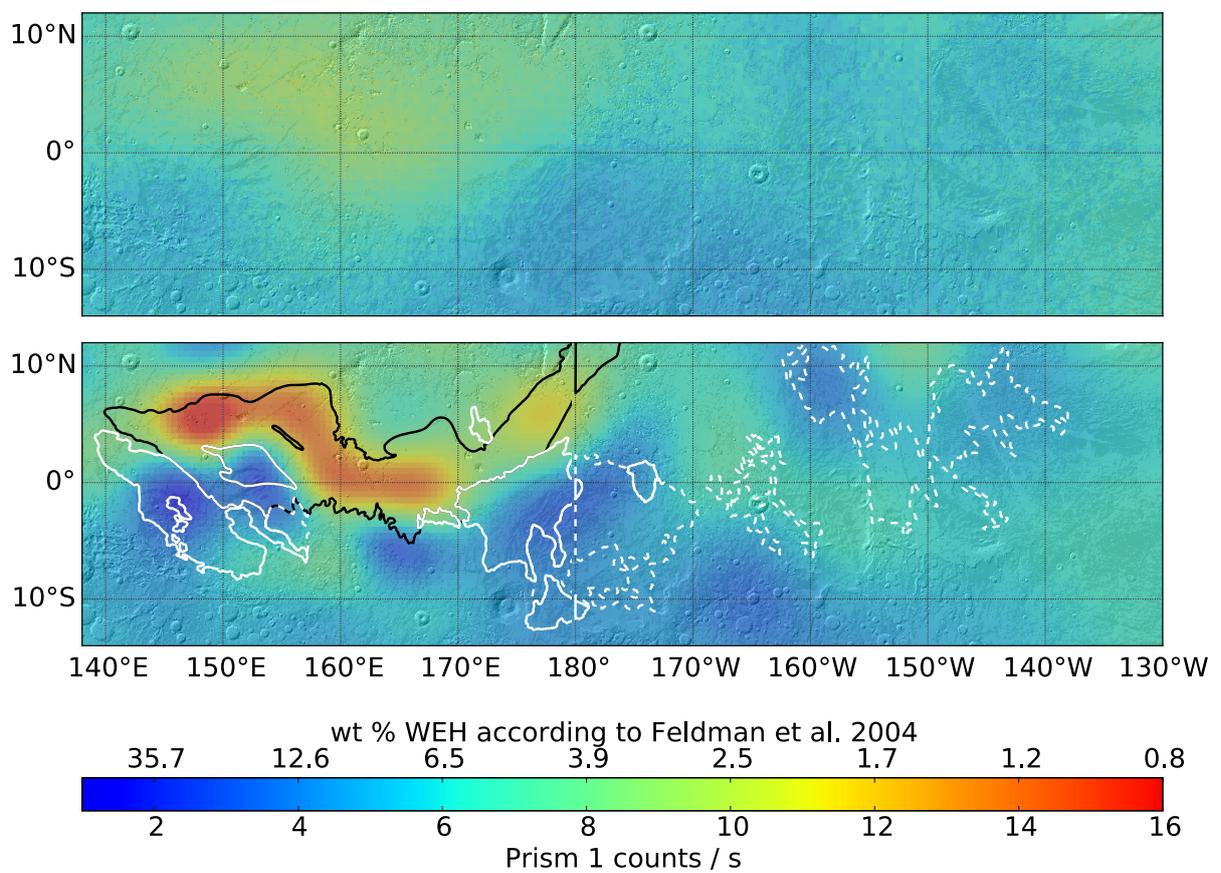
9

Figure 9: (*Top*) Raw MONS data and (*Bottom*) pixon reconstruction around the MFF. A MOLA shaded relief map is underlayed. The contours outline the young undivided channel material (black) and middle and lower members of the MFF (white solid and dashed, respectively) identified in Scott and Tanaka (1986).

up to 50 wt. % WEH, but their stability in the Martian regolith has not been demonstrated (Bish et al., 2003). No detections of hydrated minerals within the MFF are reported in either CRISM or OMEGA data sets (Carter et al., 2013).

5.2. Tropical mountain glaciers at the Tharsis Montes

The Tharsis region, shown with a black rectangle in figure 8, is presented in more detail in figure 10. In our pixon reconstruction in the right panel of figure 10, the line of the Tharsis Montes is seen to separate regions of higher and lower WEH abundances, where the north-west side of the line is enhanced in hydrogen with abundances >7 wt% WEH on the north-west flanks of the Tharsis Montes. This hydrogen concentration is greater than that in the raw data (figure 10 left panel) and than in Elphic et al. (2005a). The area with the highest WEH concentration is north-west of Olympus Mons (at 18.65° N, 134° W) and coincides with the Lycus Sulci region where the WEH content reaches 11 wt%.

In addition to these hydrogen enhancements, Forget et al. (2006) suggest that ice should condense west of Elysium Mons (25.02° N, 147.21° E) during periods of high orbital obliquity. In figure 8 we also find a decreased epithermal neutron count rate, implying enhanced WEH, at this location. Forget et al. (2006) also note that if the source for the atmospheric water during periods of high obliquity were not the north polar cap alone but included an additional, hypothetical, south polar water cap, then ice would be deposited in the Eastern Hellas basin (110°E, 40°S). However, we see no evidence for this in figure 8.

That we see a peak in the count rate in the reconstruction so closely coincident with the position of Olympus Mons in MOLA topography (figure 10) strengthens our faith in the other features shown in the reconstruction. The region of enhanced hydrogen content around Ascraeus Mons (107°W, 12°N) is larger than the glacial deposit identified by Parsons and Head (2005). This may be an interesting result, although establishing its significance will require determining the precise spatial resolution of the reconstruction at this location.

6. Other locations with evidence of present water

In this section we will examine in our pixon reconstruction of the MONS data several locations that are suggested on the basis of other spectral or imaging data to show evidence of past or present hydration. The MONS reconstruction will be used to reveal whether the top metre of the surface is hydrated at these locations today.

6.1. Elysium Planitia: ice or lava?

The Cerberus fossae are a 1600 km long set of parallel fissures at Elysium planitia, in equatorial Mars. The fissures stretch from 154.43°E, 16.16°N to 174.72°E, 6.23°N. The fault is believed to be related to the Elysium Montes, located to the northwest, and there is morphological evidence that it has been the source of both water and lava floods (Berman and Hartmann, 2002; Burr et al., 2002; Head and Marchant, 2003) within the last 2-10 Myr. It had been assumed that the water had

sublimated away, leaving only the fluvial channels of Athabasca and Marte Valles as evidence of the water flows. However, Murray et al. (2005) identified, in Mars Express High Resolution Stereo Camera (HRSC) images, plate-like features that they argued must be the remains of a buried frozen sea 800×900 km across and up to 45 m deep, centred at 5° N, 150° E. Their argument is based on three observations: the geomorphological similarities of the HRSC images with those taken above Antartica showing the break up of pack-ice, discrepancies between the ages of the plates and inter-plate regions, and the reduction in the volume of craters that have been filled by the flow.

The epithermal neutron flux is sensitive only to the top metre of the surface, which, if the frozen sea were present, may consist of sublimation lag or pyroclastic deposits from subsequent eruptions from the Cerberus fossae. Nonetheless, if the outflow occurred within the last 10 Myr we may still expect to see excess hydration due to partial protection of the water by a dust cover lag, perhaps containing hydrated mineral layers that provide a barrier protecting a deeper, higher-humidity environment (Feldman et al., 2011; Wang and Ling, 2011).

The locally adaptive pixon reconstruction of the region around the proposed, buried sea is shown in figure 9. The location of the water ice sea, 5° N, 150° E, corresponds to one of the locations with the highest epithermal neutron flux on the entire surface of Mars. This suggests that the top few tens of centimetres of soil, in this region, are unusually dry with < 1 wt. % WEH. The dry feature in the reconstruction extends beyond the region identified by Murray et al. (2005) and covers much of the smooth plains that are believed to be young basaltic lavas from Cerberus fossae (outline with a black contour in figure 9). Additionally, Boynton et al. (2007), using Mars Odyssey Gamma Ray Spectrometer data, find this region to be enhanced in Fe. Taken together, these result suggests that the plate-like features at Elysium Planitia are unlikely to be a buried water ice sea but are, instead, young, Fe-rich, volatile-poor basalts. Although no enhancement in the near-subsurface hydrogen content is seen in this region the very high epithermal neutron flux suggests that it is compositionally unique. Previous work using MONS data has considered only the effects of H and CO_2 on the epithermal neutron flux. To understand the effect of changing the abundances of other elements, such as iron, would require new neutron transport simulations.

The results of section 4.2 indicate a systematic error of up to 1.5 counts per second and a random error of 0.6 counts per second in this region. These errors are amongst the highest on the surface, however even in the worst case scenario that the random and systematic errors were in the same direction southern Elysium planitia remains an exceptionally dry region. Thus, our conclusions will not be affected, qualitatively, by errors in the reconstruction technique.

6.2. Meridiani Planum

Meridiani Planum is a plain centred at 0.2° N, 2.5° W and near the dichotomy boundary. The plains became an area of intense interest after they were identified as being one of the few locations containing, and the only large deposit of, crystalline, grey hematite on Mars (Christensen et al., 2001). The favoured
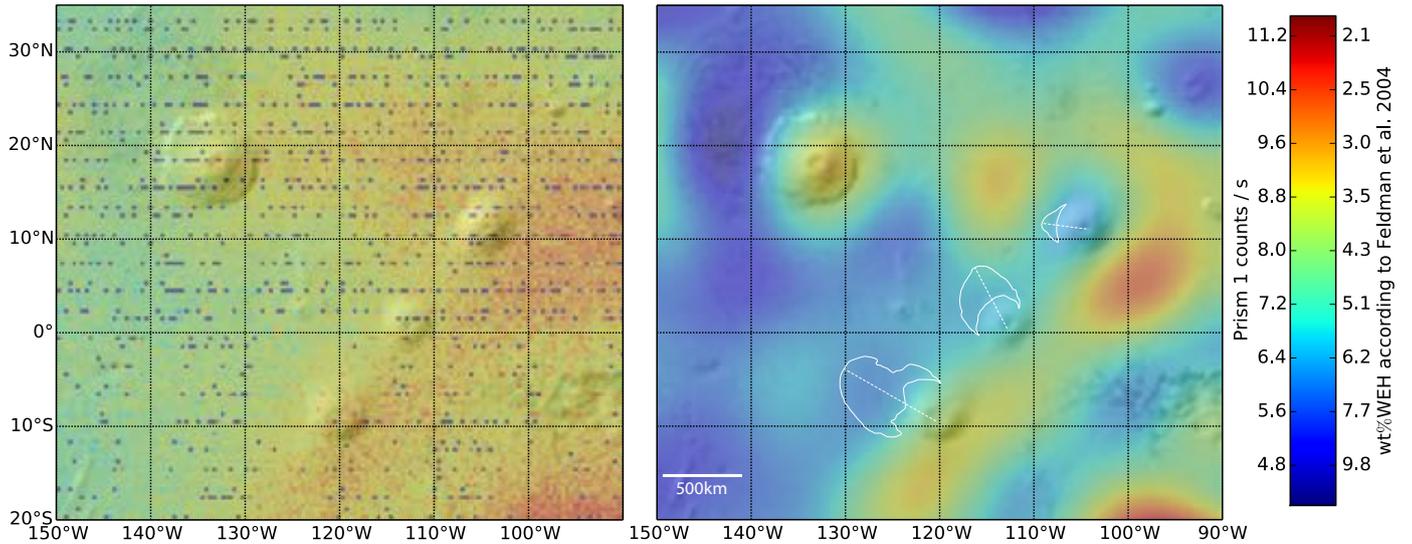
Figure 10: **Left**: Gridded MONS prism-1 data at Tharsis. **Right**: Pixon reconstruction of the MONS prism-1 data at Tharsis, showing the WEH conversion of Feldman et al. (2004b). Underlaid is a MOLA shaded relief map. The white contours show fan shaped deposits on the slopes of the Tharsis Montes (and are based on those in Fastook et al. (2008).
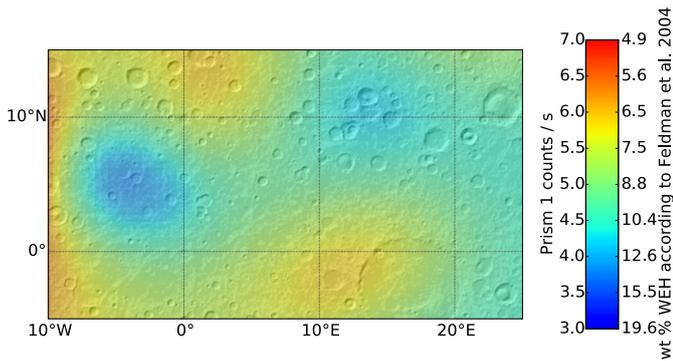

Figure 11: Locally adaptive pixon reconstruction of the MONS epithermal data around Meridiani Planum.

explanation for the origin of this mineral is chemical precipitation from aqueous Fe-rich fluids. This process requires the presence of liquid water, on the surface of Mars, for substantial periods of time, early in its history (Christensen et al., 2001). For this reason the region was selected as the landing site for NASA's Mars Exploration Rover, Opportunity.

The grey hematite deposits are centred on 4° W, 2° S. Comparison with figure 11 shows this area is not enriched in H in the MONS reconstruction. However, an area of the Planum ~600 km to the north, at 5° W, 4° N, does show hydrogen enrichment with ~15 wt. % WEH, consistent with the presence of hydrated minerals. This region was shown, using the OMEGA visible-near infrared hyperspectral imager, to contain hydrated minerals including kieserite, gypsum, and polyhydrated sulfates (Gendrin et al., 2005). Why the hematite deposits appear less hydrogen rich than hydrated mineral deposits to their north is not clear.

6.3. Recurring slope lineae

Recurring slope lineae are narrow, dark markings that appear and grow on Martian steep slopes during warm seasons and fade in cold seasons. They have been found at equatorial and mid-latitudes and were first identified using HiRISE images (McEwen et al., 2011). Contemporary liquid water activity on the surface of Mars has recently been confirmed at sites showing recurring slope lineae, using infra-red spectral data from the Compact Reconnaissance Imaging Spectrometer for Mars onboard the Mars Reconnaissance Orbiter (Ojha et al., 2015).

The origin and recharge mechanism of these liquid brines detected in recurring slope lineae (RSL) has important implications for the current Martian water cycle and budget. However the exact mechanism that recharges the RSL, which may vary across the surface, remains poorly understood. At least three possible scenarios exist: feeding from shallow briny aquifers (McEwen et al., 2011; Chevrier and Rivera-Valentin, 2012); melting of shallow ice during warm seasons (McEwen et al., 2014), which provides good temporal agreement with RSL formation but may not be able to provide suffient water over long periods (Stillman et al., 2014; Grimm et al., 2014); and absorption of atmospheric water vapour by deliquescent salts. The first two of these hypotheses require some subsurface store of water but the third does not. Additionally, a dry hypothesis involving granular flow is possible (McEwen et al., 2011).

To distinguish between these hypotheses, we use the results of our locally adaptive pixon reconstruction of the MONS epithermal neutron data.

6.3.1. Correlation of RSL position with H abundance

Comparison of the high resolution hydrogen map with the locations of RSL shows no positive correlation (figure 8). To test this comparison and find whether RSL occur in special re-
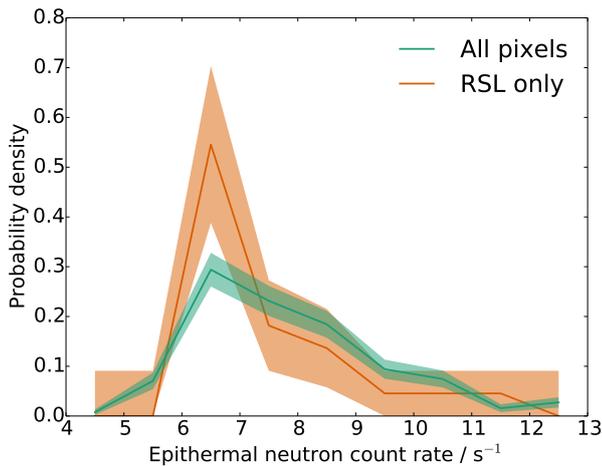
Figure 12: The probability density function of the count rate between 53°S and 30°S and just those pixels containing RSL. The translucent regions indicate 1σ errors.

gions in the WEH map we will examine the probability density function of the count rate. Figure 12 shows the probability density function of the reconstructed count rate in the southern mid-latitudes (SML), along with the probability distribution of the count rate restricted to sites within the SML containing RSL. We compared these two distributions using a two-sample Kolmogorov-Smirnov test (Press et al., 1992), which measures the maximum difference between the cumulative distribution functions of two samples. This tests the null hypothesis that the data sets are drawn from the same distribution. Large values of the test statistic imply that the two samples are not drawn from the same underlying distribution. To carry out this calculation the data were repixelated more coarsely so that adjacent pixels are effectively uncorrelated. We find a Kolmogorov-Smirnov test statistic of 0.2 and corresponding p-value of 0.2 (i.e. test statistics at least this extreme are expected 20% of the time). This is not sufficient to imply that the count-rates (and consequently water abundances) where RSL are present are different from those locations where RSL are absent. In turn, this result implies that the occurrence of RSL is independent of the WEH of the top few 10s of cm of soil on large scales. It should be noted that this analysis assumes that the distribution of discovered RSL reflects their true distribution across the surface in an unbiased way. If there are strong selection effects that correlate with WEH abundance then the results may change, for example if the low albedo regions in which RSL are found also have anomalous hydrogen abundances.

That WEH abundance in the soil is not correlated with RSL activity can be explained either by reference to the resolution of the neutron data, even at 290 km the resolution is too coarse and the regions containing RSL are blurred into those without, or we must conclude that there are no sizeable stores of subsurface water close to the RSL thus their formation and renewal is not driven by subsurface aquifers or water ice. Water buried beneath the level accessible to the MONS data (i.e. deeper than

about 1 m) could not act as a source for the RSL because thermal inertia prevents ice buried beneath 20 cm from ever being melted (Stillman et al., 2014). It was shown in section 4.2.1 that water deposits smaller than 60 km in radius do not produces statistically significant decreases in epithermal neutron count rate, so RSL sources smaller than this are not ruled out by this work.

If the RSL water were sourced from a subsurface reservoir too small to be seen in MONS data then we may expect that improving the resolution would go some way towards alleviating this discrepancy. However we find no evidence of a systematic increase in water abundance at the RSL with reconstruction. If the water source for the RSL is not subsurface then it must be either atmospheric or the sublimation of deeply buried ice deposits. But, both of these mechanisms require that the deliquescence of chlorate and perchlorate salts (the presence of which has been confirmed by CRISM and in-situ measurements (Hecht et al., 2009; Glavin et al., 2013; Ojha et al., 2015)) produces sufficient quantities of liquid brines to darken the soil and produce the RSL.

7. Conclusions

We have investigated several regions of interest across the Martian surface that have previously been hypothesised to contain water or hydrated minerals. A consequence of blurring by the detector footprint is that earlier analyses of the neutron count rates had led to underestimation of the dynamic range of hydrogen abundance in regions with local variation.

At low and equatorial latitudes we found evidence, in the reconstruction of the MONS data, for buried water ice in the Medusae Fossae Formation and on the western slopes of the Tharsis Montes and Elysium Mons. This supports the hypothesis that Mars in the recent geological past rotated on an axis highly inclined to its current one. On the other hand, the Cerberus fossae region containing plate-like features, suggested to be a buried water ice sea, was found to be exceptionally dry. Although this region seems not to contain hydrogen within the top few tens of cm of the surface, its unusually high epithermal neutron flux is consistent with the area being unusually high in Fe and low in H. Further work using Monte Carlo particle transport codes is required to learn more about the composition of this feature.

Recurring slope lineae are transient features recently discovered on Martian steep slopes during warm seasons. Their narrow, dark shapes resemble water courses – and the presence of liquid water has recently been spectroscopically confirmed near some RSL sites. Yet, if this is what they are, then their source remains unknown. We find that the hydrogen abundance, on scales of ~290 km, at RSL sites is statistically no different from anywhere else at similar latitudes. This implies that RSL are not supplied by large (> 160 km diameter), near-surface briny aquifers. Preferred hypotheses remain for RSL to either be fed by water vapour, either from sublimating deeply buried water ice or from the atmosphere, or by small (< 160 km diameter) or deeply (> 1 m) buried aquifers.

Appendix A. Convolution with an azimuthally symmetric bandlimited function

The convolution between a circularly symmetric (or zonal) function (i.e. one that depends only on arc-length from a particular point, taken to be the north pole), G, with an arbitrary function, f, defined on the sphere can be written:

$$(G * f)(\boldsymbol{\xi}) = \int_{\mathbb{S}^2} G(\boldsymbol{\xi} \cdot \boldsymbol{\xi}') f(\boldsymbol{\xi}') d\boldsymbol{\xi}' \qquad (A.1)$$

i.e. an integral over the 2-sphere.

The spherical harmonic (SH) representation of G is

$$G(\boldsymbol{\xi}) = \sum_{l=0}^{\infty} \sum_{m=-l}^{l} g_l^m Y_l^m(\boldsymbol{\xi}). \qquad (A.2)$$

As G is circular, $a_{lm} = 0$ for $m \neq 0$ thus

$$\begin{aligned} G(\boldsymbol{\xi}) &= \sum_{l=0}^{\infty} g_l^0 Y_0^l(\boldsymbol{\xi}) \\ G(\boldsymbol{\xi}) &= \sum_{l=0}^{\infty} \sqrt{\frac{2l+1}{4\pi}} g_l^0 P_l(\boldsymbol{\xi}), \end{aligned} \qquad (A.3)$$

where P_l is the lth Legendre function. substituting this back into equation (A.1) gives

$$\begin{aligned} (G * f)(\boldsymbol{\xi}) &= \sum_{l=0}^{\infty} \int_{S^2} \sqrt{\frac{2l+1}{4\pi}} g_l^0 P_l(\boldsymbol{\xi} \cdot \boldsymbol{\xi}') f(\boldsymbol{\xi}') d\boldsymbol{\xi}' \\ &= \sum_{l=0}^{\infty} \sum_{m=-l}^{l} \sqrt{\frac{4\pi}{2l+1}} g_l^0 Y_l^m(\boldsymbol{\xi}) \int_{S^2} Y_l^m(\boldsymbol{\xi}') f(\boldsymbol{\xi}') d\boldsymbol{\xi}' \\ &= \sum_{l=0}^{\infty} \sum_{m=-l}^{l} \sqrt{\frac{4\pi}{2l+1}} g_l^0 f_l^m Y_l^m(\boldsymbol{\xi}), \end{aligned}$$
$$(A.4)$$

which can be seen to be a simple scaling of the SH coefficients of the function f. These scaling factors can be calculated empirically. In the case of convolution with a Gaussian function, of width σ, the appropriate SH coefficients can be calculated by solving for the fundamental solution of the heat equation, on the sphere. We find that the appropriate solution is

$$g_l^m = \sqrt{\frac{2l+1}{4\pi}} e^{\frac{-l(l+1)\sigma^2}{2}}. \qquad (A.5)$$

This algorithm has a time complexity of $O(l_{max}^2)$, where l_{max} is the maximum order used in our spherical harmonic decompositions, so in practice will be dominated by the time taken to perform the spherical harmonic transforms of the function being convolved, which in our implementation has $O(l_{max}^3)$ complexity. This method is therefore $O(l_{max})$ faster than the 'fast' method described in the previous section and $O(l_{max}^2)$ faster than the brute force method. As, in this work, l_{max} will typically be $O(10^2)$, care will be taken to formulate the deconvolution techniques such that all convolutions are with azimuthally symmetric functions.

Appendix B. Integration of functions defined in pixel space

It should be noted that the integrations in this and the previous section are done over solid angle rather than pixels. To convert from one coordinate system to the other, note that

$$\int d\mathbf{x} = N_{\text{pix}} \qquad (B.1)$$

$$= \int \frac{\partial \mathbf{x}}{\partial \boldsymbol{\Omega}} d\boldsymbol{\Omega} \qquad (B.2)$$

$$= \int \frac{1}{a(\boldsymbol{\Omega})} d\boldsymbol{\Omega}, \qquad (B.3)$$

where $a(\boldsymbol{\Omega})$ is the area of the pixel at position $\boldsymbol{\Omega}$, which is given by

$$a(\boldsymbol{\Omega}) = a(\theta, \phi) = \Delta\phi \left(\cos\left(\theta - \frac{\Delta\theta}{2}\right) - \cos\left(\theta + \frac{\Delta\theta}{2}\right) \right). \quad (B.4)$$

$\Delta\phi$ is the width of the pixels in longitude, i.e. $\Delta\phi = \frac{2\pi}{X}$, where X is the number of pixels in the longitudinal direction, similarly, $\Delta\theta = \frac{\pi}{Y}$.

References

Berman, D. C., Hartmann, W. K., Sep. 2002. Recent Fluvial, Volcanic, and Tectonic Activity on the Cerberus Plains of Mars. Icarus159, 1–17.

Bish, D. L., William Carey, J., Vaniman, D. T., Chipera, S. J., Jul. 2003. Stability of hydrous minerals on the martian surface. Icarus164, 96–103.

Boynton, W. V., Taylor, G. J., Evans, L. G., Reedy, R. C., Starr, R., Janes, D. M., Kerry, K. E., Drake, D. M., Kim, K. J., Williams, R. M. S., Crombie, M. K., Dohm, J. M., Baker, V., Metzger, A. E., Karunatillake, S., Keller, J. M., Newsom, H. E., Arnold, J. R., Brückner, J., Englert, P. A. J., Gasnault, O., Sprague, A. L., Mitrofanov, I., Squyres, S. W., Trombka, J. I., d'Uston, L., Wänke, H., Hamara, D. K., Dec. 2007. Concentration of H, Si, Cl, K, Fe, and Th in the low- and mid-latitude regions of Mars. Journal of Geophysical Research (Planets) 112, E12S99.

Burr, D. M., Grier, J. A., McEwen, A. S., Keszthelyi, L. P., Sep. 2002. Repeated Aqueous Flooding from the Cerberus Fossae: Evidence for Very Recently Extant, Deep Groundwater on Mars. Icarus159, 53–73.

Campbell, B. A., Putzig, N. E., Carter, L. M., Morgan, G. A., Phillips, R. J., Plaut, J. J., Mar. 2013. Roughness and near-surface density of Mars from SHARAD radar echoes. Journal of Geophysical Research (Planets) 118, 436–450.

Carter, J., Poulet, F., Bibring, J.-P., Mangold, N., Murchie, S., Apr. 2013. Hydrous minerals on Mars as seen by the CRISM and OMEGA imaging spectrometers: Updated global view. Journal of Geophysical Research (Planets) 118, 831–858.

Chevrier, V. F., Rivera-Valentin, E. G., Nov. 2012. Formation of recurring slope lineae by liquid brines on present-day Mars. Geophys. Res. Lett.39, 21202.

Christensen, P. R., Morris, R. V., Lane, M. D., Bandfield, J. L., Malin, M. C., Oct. 2001. Global mapping of Martian hematite mineral deposits: Remnants of water-driven processes on early Mars. Journal of Geophysical Research (Planets)106, 23873–23886.

Dundas, C. M., McEwen, A. S., Jul. 2015. Slope activity in Gale crater, Mars. Icarus254, 213–218.

Eke, V., Jun. 2001. A speedy pixon image reconstruction algorithm. MN-RAS324, 108–118.

Eke, V. R., Teodoro, L. F. A., Elphic, R. C., Mar. 2009. The spatial distribution of polar hydrogen deposits on the Moon. Icarus200, 12–18.

Elphic, R. C., Eke, V. R., Teodoro, L. F. A., Lawrence, D. J., Bussey, D. B. J., Jul. 2007. Models of the distribution and abundance of hydrogen at the lunar south pole. Geophys. Res. Lett.34, 13204.

Elphic, R. C., Feldman, W. C., Prettyman, T. H., Tokar, R. L., Lawrence, D. J., Head, III, J. W., Maurice, S., Mar. 2005. Mars Odyssey Neutron Spectrometer Water-Equivalent Hydrogen: Comparison with Glacial Landforms on Tharsis. In: Mackwell, S., Stansbery, E. (Eds.), 36th Annual Lunar and Planetary Science Conference. Vol. 36 of Lunar and Planetary Science Conference.

Fastook, J. L., Head, J. W., Marchant, D. R., Forget, F., Dec. 2008. Tropical mountain glaciers on Mars: Altitude-dependence of ice accumulation, accumulation conditions, formation times, glacier dynamics, and implications for planetary spin-axis/orbital history. Icarus198, 305–317.

Feldman, W. C., Boynton, W. V., Tokar, R. L., Prettyman, T. H., Gasnault, O., Squyres, S. W., Elphic, R. C., Lawrence, D. J., Lawson, S. L., Maurice, S., McKinney, G. W., Moore, K. R., Reedy, R. C., Jul. 2002. Global Distribution of Neutrons from Mars: Results from Mars Odyssey. Science 297, 75–78.

Feldman, W. C., Head, J. W., Maurice, S., Prettyman, T. H., Elphic, R. C., Funsten, H. O., Lawrence, D. J., Tokar, R. L., Vaniman, D. T., Sep. 2004a. Recharge mechanism of near-equatorial hydrogen on Mars: Atmospheric redistribution or sub-surface aquifer. Geophys. Res. Lett.31, L18701.

Feldman, W. C., Pathare, A., Maurice, S., Prettyman, T. H., Lawrence, D. J., Milliken, R. E., Travis, B. J., Nov. 2011. Mars Odyssey neutron data: 2. Search for buried excess water ice deposits at nonpolar latitudes on Mars. Journal of Geophysical Research (Planets) 116, E11009.

Feldman, W. C., Prettyman, T. H., Maurice, S., Plaut, J. J., Bish, D. L., Vaniman, D. T., Mellon, M. T., Metzger, A. E., Squyres, S. W., Karunatillake, S., Boynton, W. V., Elphic, R. C., Funsten, H. O., Lawrence, D. J., Tokar, R. L., Sep. 2004b. Global distribution of near-surface hydrogen on Mars. Journal of Geophysical Research (Planets) 109, 9006.

Forget, F., Haberle, R. M., Montmessin, F., Levrard, B., Head, J. W., Jan. 2006. Formation of Glaciers on Mars by Atmospheric Precipitation at High Obliquity. Science 311, 368–371.

Gendrin, A., Mangold, N., Bibring, J.-P., Langevin, Y., Gondet, B., Poulet, F., Bonello, G., Quantin, C., Mustard, J., Arvidson, R., Le Mouélic, S., Mar. 2005. Sulfates in Martian Layered Terrains: The OMEGA/Mars Express View. Science 307, 1587–1591.

Glavin, D. P., Freissinet, C., Miller, K. E., Eigenbrode, J. L., Brunner, A. E., Buch, A., Sutter, B., Archer, P. D., Atreya, S. K., Brinckerhoff, W. B., Cabane, M., Coll, P., Conrad, P. G., Coscia, D., Dworkin, J. P., Franz, H. B., Grotzinger, J. P., Leshin, L. A., Martin, M. G., McKay, C., Ming, D. W., Navarro-González, R., Pavlov, A., Steele, A., Summons, R. E., Szopa, C., Teinturier, S., Mahaffy, P. R., Oct. 2013. Evidence for perchlorates and the origin of chlorinated hydrocarbons detected by SAM at the Rocknest aeolian deposit in Gale Crater. Journal of Geophysical Research (Planets) 118, 1955–1973.

Greeley, R., Guest, J. E., 1987. Geologic map of the eastern equatorial region of mars. Tech. rep.
URL http://pubs.er.usgs.gov/publication/i1802B

Grimm, R. E., Harrison, K. P., Stillman, D. E., May 2014. Water budgets of martian recurring slope lineae. Icarus233, 316–327.

Head, J. W., Marchant, D. R., Jul. 2003. Cold-based mountain glaciers on Mars: Western Arsia Mons. Geology 31, 641.

Head, J. W., Weiss, D. K., Nov. 2014. Preservation of ancient ice at Pavonis and Arsia Mons: Tropical mountain glacier deposits on Mars. Planetary and Space Science103, 331–338.

Head, III, J. W., Kreslavsky, M., Mar. 2004. Medusae Fossae Formation: Ice-rich Airborne Dust Deposited During Periods of High Obliquity? In: Mackwell, S., Stansbery, E. (Eds.), Lunar and Planetary Science Conference. Vol. 35 of Lunar and Planetary Science Conference.

Hecht, M. H., Kounaves, S. P., Quinn, R. C., West, S. J., Young, S. M. M., Ming, D. W., Catling, D. C., Clark, B. C., Boynton, W. V., Hoffman, J., DeFlores, L. P., Gospodinova, K., Kapit, J., Smith, P. H., Jul. 2009. Detection of Perchlorate and the Soluble Chemistry of Martian Soil at the Phoenix Lander Site. Science 325, 64–.

Laskar, J., Correia, A. C. M., Gastineau, M., Joutel, F., Levrard, B., Robutel, P., Aug. 2004. Long term evolution and chaotic diffusion of the insolation quantities of Mars. Icarus170, 343–364.

Lawrence, D. J., Puetter, R. C., Elphic, R. C., Feldman, W. C., Hagerty, J. J., Prettyman, T. H., Spudis, P. D., Feb. 2007. Global spatial deconvolution of Lunar Prospector Th abundances. Geophys. Res. Lett.34, 3201.

Madeleine, J.-B., Forget, F., Head, J. W., Levrard, B., Montmessin, F., Millour, E., Oct. 2009. Amazonian northern mid-latitude glaciation on Mars: A proposed climate scenario. Icarus203, 390–405.

Maurice, S., Feldman, W., Diez, B., Gasnault, O., Lawrence, D. J., Pathare, A., Prettyman, T., Nov. 2011. Mars Odyssey neutron data: 1. Data processing and models of water-equivalent-hydrogen distribution. Journal of Geophysical Research (Planets) 116, 11008.

Maurice, S., Lawrence, D. J., Feldman, W. C., Elphic, R. C., Gasnault, O., Jun. 2004. Reduction of neutron data from Lunar Prospector. Journal of Geophysical Research (Planets) 109, E07S04.

McEwen, A. S., Dundas, C. M., Mattson, S. S., Toigo, A. D., Ojha, L., Wray, J. J., Chojnacki, M., Byrne, S., Murchie, S. L., Thomas, N., 01 2014. Recurring slope lineae in equatorial regions of mars. Nature Geosci 7 (1), 53–58.
URL http://dx.doi.org/10.1038/ngeo2014

McEwen, A. S., Ojha, L., Dundas, C. M., Mattson, S. S., Byrne, S., Wray, J. J., Cull, S. C., Murchie, S. L., Thomas, N., Gulick, V. C., Aug. 2011. Seasonal Flows on Warm Martian Slopes. Science 333, 740–.

Mellon, M. T., Jakosky, B. M., Feb. 1993. Geographic variations in the thermal and diffusive stability of ground ice on Mars. Journal of Geophysical Research (Planets)98, 3345–3364.

Mitrofanov, I. G., Kozyrev, A. S., Lisov, D. I., Vostrukhin, A. A., Golovin, D. V., Litvak, M. L., Malakhov, A. V., Mokrousov, M. I., Nikiforov, S. Y., Sanin, A. B., Apr. 2016. Active neutron sensing of the Martian surface with the DAN experiment onboard the NASA "Curiosity" Mars rover: Two types of soil with different water content in the gale crater. Astronomy Letters 42, 251–259.

Mitrofanov, I. G., Litvak, M. L., Sanin, A. B., Starr, R. D., Lisov, D. I., Kuzmin, R. O., Behar, A., Boynton, W. V., Hardgrove, C., Harshman, K., Jun, I., Milliken, R. E., Mischna, M. A., Moersch, J. E., Tate, C. G., Jul. 2014. Water and chlorine content in the Martian soil along the first 1900 m of the Curiosity rover traverse as estimated by the DAN instrument. Journal of Geophysical Research (Planets) 119, 1579–1596.

Mitrofanov, I. G., Litvak, M. L., Varenikov, A. B., Barmakov, Y. N., Behar, A., Bobrovnitsky, Y. I., Bogolubov, E. P., Boynton, W. V., Harshman, K., Kan, E., Kozyrev, A. S., Kuzmin, R. O., Malakhov, A. V., Mokrousov, M. I., Ponomareva, S. N., Ryzhkov, V. I., Sanin, A. B., Smirnov, G. A., Shvetsov, V. N., Timoshenko, G. N., Tomilina, T. M., Tret'yakov, V. I., Vostrukhin, A. A., Sep. 2012. Dynamic Albedo of Neutrons (DAN) Experiment Onboard NASA's Mars Science Laboratory. Space Sci. Rev.170, 559–582.

Murray, J. B., Muller, J.-P., Neukum, G., Werner, S. C., van Gasselt, S., Hauber, E., Markiewicz, W. J., Head, J. W., Foing, B. H., Page, D., Mitchell, K. L., Portyankina, G., HRSC Co-Investigator Team, Mar. 2005. Evidence from the Mars Express High Resolution Stereo Camera for a frozen sea close to Mars' equator. Nature434, 352–356.

Ojha, L., Wilhelm, M. B., Murchie, S. L., McEwen, A. S., Wray, J. J., Hanley, J., Masse, M., Chojnacki, M., 11 2015. Spectral evidence for hydrated salts in recurring slope lineae on mars. Nature Geosci 8 (11), 829–832.
URL http://dx.doi.org/10.1038/ngeo2546

Parsons, R. L., Head, III, J. W., Mar. 2005. Ascraeus Mons Fan-shaped Deposit, Mars: Geological History and Volcano-Ice Interactions of a Cold-

based Glacier. In: Mackwell, S., Stansbery, E. (Eds.), 36th Annual Lunar and Planetary Science Conference. Vol. 36 of Lunar and Planetary Science Conference.

Pina, R. K., Puetter, R. C., Nov. 1992. Incorporation of Spatial Information in Bayesian Image Reconstruction: The Maximum Residual Likelihood Criterion. PASP104, 1096.

Pina, R. K., Puetter, R. C., Jun. 1993. Bayesian image reconstruction - The pixon and optimal image modeling. PASP105, 630–637.

Press, W. H., Teukolsky, S. A., Vetterling, W. T., Flannery, B. P., 1992. Numerical recipes in C. The art of scientific computing.

Prettyman, T. H., Feldman, W. C., Titus, T. N., Aug. 2009. Characterization of Mars' seasonal caps using neutron spectroscopy. Journal of Geophysical Research (Planets) 114, 8005.

Schorghofer, N., Sep. 2007. Dynamics of ice ages on Mars. Nature449, 192–194.

Schorghofer, N., Aharonson, O., May 2005. Stability and exchange of subsurface ice on Mars. Journal of Geophysical Research (Planets) 110, E05003.

Schultz, P., Lutz, A. B., Jan. 1988. Polar wandering of Mars. Icarus73, 91–141.

Scott, D. H., Tanaka, K. L., Feb. 1982. Ignimbrites of Amazonis Planitia region of Mars. Journal of Geophysical Research (Planets)87, 1179–1190.

Scott, D. H., Tanaka, K. L., 1986. Geologic map of the western equatorial region of mars. Tech. rep.
URL http://pubs.er.usgs.gov/publication/i1802A

Shean, D. E., Head, J. W., Fastook, J. L., Marchant, D. R., Mar. 2007. Recent glaciation at high elevations on Arsia Mons, Mars: Implications for the formation and evolution of large tropical mountain glaciers. Journal of Geophysical Research (Planets) 112, E03004.

Shean, D. E., Head, J. W., Marchant, D. R., May 2005. Origin and evolution of a cold-based tropical mountain glacier on Mars: The Pavonis Mons fan-shaped deposit. Journal of Geophysical Research (Planets) 110, E05001.

Squyres, S., 2011. The National Academies press, Washington DC.

Stillman, D. E., Michaels, T. I., Grimm, R. E., Hanley, J., Feb. 2016. Observations and modeling of northern mid-latitude recurring slope lineae (RSL) suggest recharge by a present-day martian briny aquifer. Icarus265, 125–138.

Stillman, D. E., Michaels, T. I., Grimm, R. E., Harrison, K. P., May 2014. New observations of martian southern mid-latitude recurring slope lineae (RSL) imply formation by freshwater subsurface flows. Icarus233, 328–341.

Teodoro, L. F. A., Elphic, R. C., Eke, V. R., Feldman, W. C., Sylvestre, M., Mar. 2013. A Global High Resolution Map of the Martian Hydrogen Distribution. In: Lunar and Planetary Science Conference. Vol. 44 of Lunar and Planetary Inst. Technical Report. p. 2623.

Tokar, R. L., Feldman, W. C., Prettyman, T. H., Moore, K. R., Lawrence, D. J., Elphic, R. C., Kreslavsky, M. A., Head, J. W., Mustard, J. F., Boynton, W. V., Oct. 2002. Ice concentration and distribution near the south pole of Mars: Synthesis of odyssey and global surveyor analyses. Geophys. Res. Lett.29, 10–1.

Wang, A., Ling, Z. C., Mar. 2011. Ferric sulfates on Mars: A combined mission data analysis of salty soils at Gusev crater and laboratory experimental investigations. Journal of Geophysical Research (Planets) 116, E00F17.

Watters, T. R., Campbell, B., Carter, L., Leuschen, C. J., Plaut, J. J., Picardi, G., Orosei, R., Safaeinili, A., Clifford, S. M., Farrell, W. M., Ivanov, A. B., Phillips, R. J., Stofan, E. R., Nov. 2007. Radar Sounding of the Medusae Fossae Formation Mars: Equatorial Ice or Dry, Low-Density Deposits? Science 318, 1125.

Wilson, J. T., Eke, V. R., Massey, R. J., Elphic, R. C., Jolliff, B. L., Lawrence, D. J., Llewellin, E. W., McElwaine, J. N., Teodoro, L. F. A., Jan. 2015. Evidence for explosive silicic volcanism on the Moon from the extended distribution of thorium near the Compton-Belkovich Volcanic Complex. Journal of Geophysical Research (Planets) 120, 92–108.